

# CENN: a fully convolutional neural network for CMB recovery in realistic microwave sky simulations

Casas J. M.<sup>1,2</sup>, Bonavera L.<sup>1,2</sup>, González-Nuevo J.<sup>1,2</sup>, Baccigalupi, C.<sup>3,4,5</sup>, Cueli M. M.<sup>1,2</sup>, Crespo D.<sup>1,2</sup>, Goitia E.<sup>1</sup>, Santos J. D.<sup>1,2</sup>, Sánchez M. L.<sup>1,2</sup>, de Cos F. J.<sup>2,6</sup>

<sup>1</sup>Departamento de Física, Universidad de Oviedo, C. Federico García Lorca 18, 33007 Oviedo, Spain  
e-mail: casasjm@uniovi.es

<sup>2</sup>Instituto Universitario de Ciencias y Tecnologías Espaciales de Asturias (ICTEA), C. Independencia 13, 33004 Oviedo, Spain

<sup>3</sup>SISSA, Via Bonomea 265, 34136 Trieste, Italy

<sup>4</sup>IFPU - Institute for fundamental physics of the Universe, Via Beirut 2, 34014 Trieste, Italy

<sup>5</sup>INFN-Sezione di Trieste, via Valerio 2, 34127 Trieste, Italy

<sup>6</sup>Escuela de Ingeniería de Minas, Energía y Materiales Independencia 13, 33004 Oviedo, Spain

June 22, 2022

## ABSTRACT

**Context.** Component separation is the process to extract the sources of emission in astrophysical maps generally by taking into account multi-frequency information. Developing more reliable methods to perform component separation is crucial for future cosmic microwave background (CMB) experiments such as the Simons Observatory, the CMB-S4 or the LiteBIRD satellite.

**Aims.** We aim to develop a machine learning method based on fully convolutional neural networks called the Cosmic microwave background Extraction Neural Network (CENN) in order to extract the CMB signal in total intensity by training the network with realistic simulations. The frequencies used are the *Planck* channels 143, 217 and 353 GHz, and we validate the neural network at all sky, and at three latitude intervals:  $0^\circ < |b| < 5^\circ$ ,  $5^\circ < |b| < 30^\circ$  and  $30^\circ < |b| < 90^\circ$ . Moreover, we do not use any Galactic or point source masks.

**Methods.** To train the neural network, we produce multi-frequency realistic simulations in the form of patches of  $256 \times 256$  pixels, which contain the CMB signal, the Galactic thermal dust, CIB and PS emissions, the thermal Sunyaev-Zel'dovich effect from galaxy clusters and the instrumental noise. After validate the network, we compare the power spectrum from input and output maps. We analyse the power spectrum from the residuals at each latitude interval and at all sky and we study the performance of our model dealing with high contamination at small scales.

**Results.** We obtain a CMB power spectrum with a mean difference between input and output of  $13 \pm 113 \mu K^2$  for multipoles up to above 4 000. We compute the residuals, obtaining  $700 \pm 60 \mu K^2$  for  $0^\circ < |b| < 5^\circ$ ,  $80 \pm 30 \mu K^2$  for  $5^\circ < |b| < 30^\circ$  and  $30 \pm 20 \mu K^2$  for  $30^\circ < |b| < 90^\circ$  for multipoles up to above 4 000. For all sky, we obtain  $30 \pm 10 \mu K^2$  for  $l \leq 1000$  and  $20 \pm 10 \mu K^2$  for  $l \leq 4000$ . We validate the neural network in a single patch with strong contamination at small scales, obtaining a difference between input and output of  $50 \pm 120 \mu K^2$  and residuals of  $40 \pm 10 \mu K^2$  up to  $l \sim 2 500$ . In all cases the uncertainty of each measure is taken as the standard deviation.

**Conclusions.** Based on the results, fully convolutional neural networks are promising methods to perform component separation in future CMB experiments. Moreover, we show that CENN is reliable against different levels of contamination from Galactic and point source foregrounds at both large and small scales.

**Key words.** Techniques: image processing – cosmic background radiation – Submillimeter: general

## 1. Introduction

The cosmic microwave background (CMB) is the relic emission from the primordial Universe at an age of about 380 000 years, an epoch called recombination (Schneider 2006). As a first approximation is homogeneous and isotropic. However, it has small deviations in intensity (temperature) and polarization from point to point in the sky called anisotropies. They were firstly detected by the Cosmic Background Explorer satellite (COBE, Smoot et al. 1992) which allow to fit the cosmological parameters and cemented the gravitational instability paradigm within a cold dark matter model. After that, the *Wilkinson* Microwave Anisotropy Probe (WMAP, Bennett et al. 2003) showed that the fluctuations are predominantly adiabatic. Finally, *Planck* (Planck Collaboration et al. 2020a), with higher angular resolution than

its antecessors, obtained a more precise CMB signal for both intensity and polarization.

The CMB anisotropies are one of the most important fields of research in modern cosmology. They are divided into two: the primary anisotropies, which are temperature fluctuations originated during recombination while secondary anisotropies are the ones due to distortions of photons through their propagation along the Universe from the recombination epoch. They can be studied by estimating the CMB power spectra, which describes the amplitude of the fluctuations  $l(l+1)C_l$  on an angular scale  $\theta \sim \pi/l = 180^\circ/l$ .

Before recombination, photons and baryons are a tightly coupled photon-baryon fluid (Peebles & Yu 1970) that oscillates relativistically causing a first peak at  $l_1 \sim 200$  and additional maxima at approximately integer multiples of  $l_1$ , called acoustic

peaks, which provide fundamental information about cosmology and, in particular, on the initial conditions and the energy contents of the Universe. Therefore, it is very important to measure them with the highest precision, implying a very precise recovery of the CMB signal. However, CMB measurements are contaminated by other signals called foregrounds.

The process to clean the microwave maps in order to recover the CMB signal is called component separation (Baccigalupi 2003), and usually exploits multi-frequency sky maps to extract cosmological information. Our work focuses at *Planck* central wavelengths, where the foregrounds are divided into two categories: firstly, diffuse emission from our Galaxy, mostly dominated by thermal dust emission (Finkbeiner et al. 1999), being the main contaminant at large angular scales. Secondly, extragalactic foregrounds such as proto-spheroidal galaxies forming the cosmic infrared background (Dole et al. 2006), radio galaxies (de Zotti et al. 2010) and infrared (IR) dusty galaxies in the process of forming their stellar masses (Toffolatti et al. 1998), and also both thermal and kinetic Sunyaev-Zeldovich effects from galaxy clusters (Carlstrom et al. 2002).

Component separation was one of the central objectives of the *Planck* mission (Leach et al. 2008, 2016b, 2016a), where four different methods were used. They were chosen because each of the selected method rely on a different class of algorithms (i.e. blind and non-blind methods, pixel-based and harmonic-based methods). The first one was NILC (Delabrouille et al. 2009), which makes minimal assumptions for the foregrounds in order to minimise the variance of the CMB using a wavelet on the sphere on the internal linear combination (ILC) algorithm. The second was SEVEM (Martínez-González et al. 2003) which is a template-based method that removes foreground contamination from the CMB-dominant bands from the lowest and highest frequency channels. The third one was based on a Bayesian parameter estimation techniques called Commander (Eriksen et al. 2006) and the fourth method was SMICA; (Delabrouille et al. 2003), a parametric approach that allows to fit the amplitude and spectral parameters of CMB and foregrounds. The main issue for the four methods is that they perform by masking both the Galactic plane and the point sources, in order to avoid their contamination. Their final confidence mask in total intensity keeps the 78% of the sky. Moreover, the implementation of such methods required years of research and developing in order to reach the current precise CMB measurement, with the introduction of notable improvements from the early to latest releases. It is the not always straightforward application of traditional methods that drives our interest in trying a different approach to component separation.

The amount of data in the last years has been produced a high impact in fields such as astrophysics and cosmology. It is necessary to develop automatic and reliable methods to perform on new data. The most promising methods are the ones based on machine learning (ML) since once they are trained, they can be validated on new data, providing results in a much shorter period of computational time with respect to whole process of traditional approaches. One of the most important ML methods are artificial neural networks, a mathematical approaches inspired on neuroscience, that can optimize models with non-linear behaviors. Some recent applications in cosmology were in the PS detection field, both in single-frequency (Bonavera et al. 2021) and in multi-frequency (Casas, J. M. et al. 2022) approaches. Moreover, they have been used in the statistical study of the CMB for extending foreground models to sub-degree angular scales (Krachmalnicoff & Puglisi 2021) and to perform a foreground model recognition for B-mode observations (Farsian

et al. 2020). They also have been used in similar works than ours for CMB recovery and thermal dust cleaning in Petroff et al. 2020 and Wang et al. 2022, an all sky approximation for multipoles up to  $l \sim 900$  in the first case, and in 2D patches for multipoles up to  $l \sim 1500$  in the second one. Another timely application is the model by Jeffrey et al. 2022, a Moment Network for polarised foreground removal using a single training image.

The aim of this work is to train our fully convolutional neural network, called the Cosmic microwave background extraction neural network (CENN), which is publicly available<sup>1</sup>, for the recovery of the CMB signal with realistic microwave sky simulations in total intensity to check the potential of the method, dealing with polarisation data in an upcoming work. The typical application of FCN is in the Euclidean space, i.e. to flat images. Obviously, this allows the CMB power spectrum estimation only down to angular scales allowed by the patch dimension. Such small patches approach might be directly applied to ground based experiments that will observe limited regions of the sky (e.g. the Simons Observatory and CMB-S4, Ade et al. 2019; Abazajian et al. 2019) In the future, for full sky coverage experiments (e.g. the LiteBIRD satellite, Sugai et al. 2020), it would be useful to apply FCN to the Hierarchical Equal Area Latitude Pixelization scheme (HEALPix, Górski et al. 2005) using for example the approach by Krachmalnicoff & Tomasi (2019).

The outline of this paper is the following. Section 2 covers how the simulated maps are generated. Section 3 describes our methodology. The results are explained in Section 4 and our conclusions are discussed in Section 5.

## 2. Simulations

To train CENN, we use realistic simulations of the microwave sky. Each simulation is formed by sky patches at the central channels of the *Planck* mission: 143, 217 and 353 GHz. Each patch has an area of  $256 \times 256$  pixels, in order to have good statistics with the shortest possible computation time. The pixel size is 90 arcsec, a number close to the 1.72 arcmin used in the *Planck* mission, which correspond to  $N_{\text{side}} = 2048$  in the HEALPix all sky pixelization schema. The maps are randomly simulated at any position in the sky, without the use of any PS or Galactic masks, and they are selected in such a way that the probability of having two exact sky maps is negligible. We simulate different datasets: one formed by 60 000 simulations used for training, another one with 6 000 simulations to evaluate the model during that training, and validation datasets with simulations apart from the train one in order to see how CENN performs on new data. The first one consists of 6 000 simulations of patches centered at any position in the sky (all sky case). Other three datasets of 2 000 simulations each are built with patches centered at three different latitude intervals:  $0^\circ < |b| < 5^\circ$  (inner Galactic region),  $5^\circ < |b| < 30^\circ$  (intermediate Galactic region) and  $30^\circ < |b| < 90^\circ$  (extragalactic region).

First, the CMB signal is projected from all sky simulations available in the Planck Legacy Archive (PLA<sup>2</sup>), which were produced using the Planck Sky Model software (PSM, Delabrouille et al. 2013). The CMB signal used in the train and test datasets is from a different PLA simulation with respect to the one used in the validation one.

As Galactic foregrounds, we assume that only thermal dust emission is contaminating the CMB, and we consider it by

<sup>1</sup> [https://github.com/jcasas4/CENN\\_Total\\_Intensity](https://github.com/jcasas4/CENN_Total_Intensity)

<sup>2</sup> <http://pla.esac.esa.int/pla/#home>

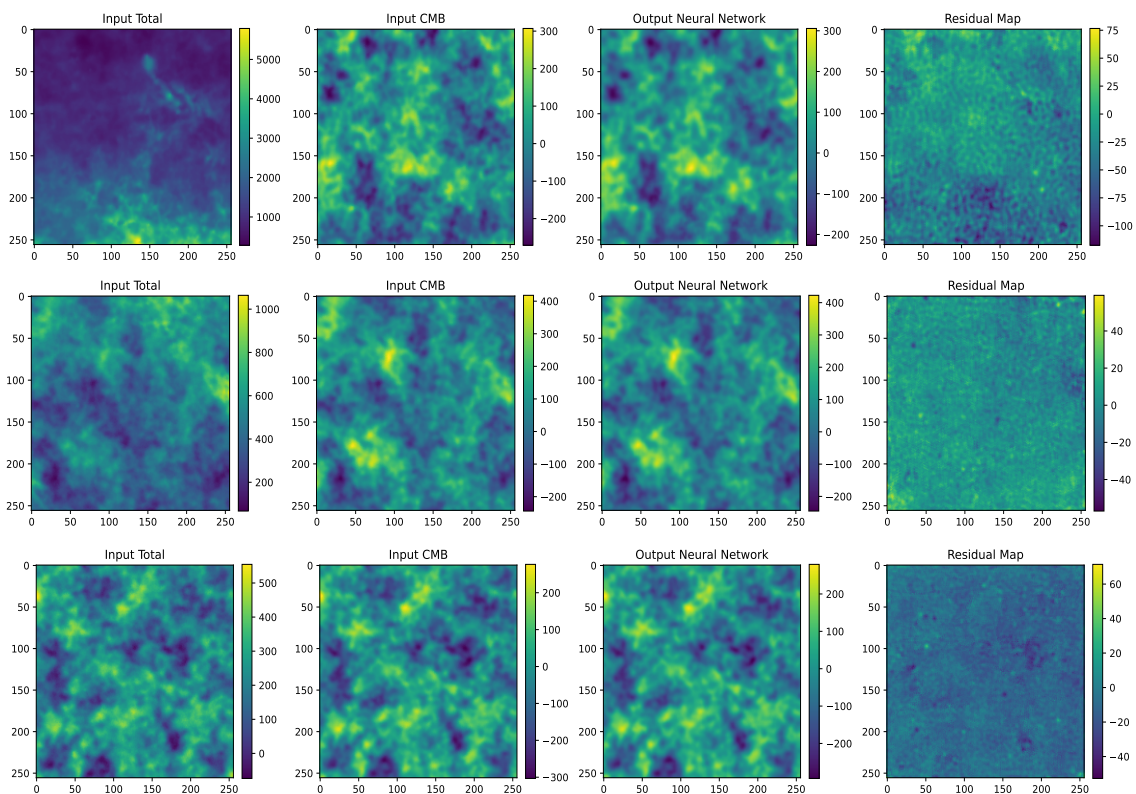


**Fig. 1.** Patches at  $0^\circ < |b| < 5^\circ$  (top row),  $5^\circ < |b| < 30^\circ$  (middle row) and  $30^\circ < |b| < 90^\circ$  (bottom row) latitude intervals. They represent the maps with all the emissions, the CMB label, the neural network output and the residual map computed as the difference between the second and the third column patches from left to right. The frequency is 217 GHz and their temperature (in  $\mu K_{CMB}$ ) is shown in their right vertical bars. The  $x$  and  $y$  labels are the pixel coordinates for each  $256 \times 256$  patch.

adding FFP10 PLA simulations from the 3<sup>rd</sup> Planck release. Although it is a good modelling at first approximation, there are studies which predict significant variations of the two modified blackbodies model of the simulations used in this work (Boudet et al. 2005, Meny et al. 2007, Paradis et al. 2011), which affect directly the behaviour of dust at small scales, neglecting the real non-Gaussian structures of this foreground.

As extragalactic foregrounds, firstly, the thermal Sunyaev-Zel'dovich effect produced by galaxy clusters is also taken into account also by using FFP10 PLA simulations. Furthermore, point sources (PS) are added as two different populations: the first one consists of radio galaxies, mainly radio quasars and BL Lacertae objects, commonly known as blazars, which are simulated at the central channel (i.e 217 GHz) following the model by Tucci et al. 2011 with the software CORRSKY (González-Nuevo et al. 2005). The second one contains infrared late-type galaxies, mainly starburst and local spiral galaxies (IRLT), which are simulated with CORRSKY at the central channel using the model by Cai et al. 2013 and normalised following the update by Negrello et al. 2013. Their spectral behavior is considered as done in Casas, J. M. et al. 2022 by assuming that their emission at 143 and 353 GHz vary as

$$S = S_0 \left( \frac{\nu}{\nu_0} \right)^\alpha, \quad (1)$$

where  $S$  is the flux density of the sources at each frequency  $\nu$ ,  $S_0$  is the flux density at the central channel with frequency  $\nu_0$ , and  $\alpha$  is the spectral index, which is randomly selected for each population using the distributions given in Planck Collaboration et al. 2016c.

Proto-spheroidal galaxies (Lapi et al. 2006) are also considered as the elements forming the cosmic infrared background (CIB, (Dole et al. 2006)), a main contaminant at high frequencies. They are simulated using the source number counts given by Cai et al. 2013, the angular power spectrum obtained by Lapi et al. 2011 and the software CORRSKY. Their spectral behavior is also considered following equation (1), assuming that they have the same spectral index distribution as for the IRLT population.

Finally, instrumental noise is added to the total input maps in order to simulate the *Planck* HFI instrument. Therefore, we use 0.55, 0.78 and 2.56  $\mu K_{CMB}$  deg values for 143, 217 and 353 GHz respectively (Planck Collaboration et al. 2018).

Each simulation is formed by two different set of maps called the input total images and the labels. The first ones are multi-frequency realistic simulations of the microwave sky at 143, 217 and 353 GHz formed by the CMB added to other signals acting as contaminants, while the labels are maps with only the CMB signal at 217 GHz. To project the maps into flat patches, the `gnomview` function of `HEALPix` framework is used. An example of simulations at different latitudes is shown in the first two columns of Figure 1 for 217 GHz. The first column represent the total input images with both the CMB signal and the other contaminants, while the second column show the CMB label maps.

### 3. Methodology

Machine learning is the ability of a computer program to learn from experience some class of tasks and performance measures. Neural networks are one of the most popular machine learning methodologies. They are inspired on neuroscience and they are

generally used to learn non-linear parameters in a model. They are usually composed by connected layers with basic computing units called neurons, which adjust their weights and bias values on each step of training.

One of the most popular applications of neural networks is to learn patterns in images to perform a detection using a special type of architecture called convolutional neural networks (LeCun et al. 1989). Image segmentation is an evolution of this task since it consist on classifying each pixel instead of the whole image. This allows to separate one class from the others. Fully-convolutional neural networks (FCN, Long et al. 2015) are the models used to perform image segmentation. They learn parameters by extracting the main features of an image through a set of convolutional blocks, while they make prediction through a set of deconvolutional blocks. As for the convolutional neural networks, each convolutional block is formed by a layer which reads information from a matrix of input data, and after that, it performs convolutions in parallel. A set of activation functions linearize the convolutions, and a pooling layer aggregates information by grouping neighbouring pixels using their local statistics. Deconvolutional blocks have a similar architecture than convolutional ones, but in this case the linearized information is deconvolved, resulting in a segmentation of the class that we want the neural network to learn.

FCN, as others neural networks, learn by performing optimisation through minimising a loss function located at the end of their architecture, a process called forward propagation. To drive the loss function to a minimum, a gradient-based optimizer is used on a small set of samples from the training dataset called minibatch. When the gradient is updated, the model parameters, which adjust some components of the architecture known as the filters, the weights or the bias, are also updated, a process called back propagation (Rumelhart et al. 1986), resulting in a theoretical better knowledge of the information read on each epoch, which is the interval when the entire train dataset flows forward and backward the neural network.

### 3.1. The model

On the one hand, our model is based on the physical assumptions explained in Eriksen et al. 2006, 2008. On the other hand, it follows the mathematical behaviors of CNN and FCN, which are extensively revised in Rumelhart et al. 1986, Lecun et al. 1998 and Goodfellow et al. 2016. In this subsection we will explain the physical concepts of our model, while the mathematical ones are summarized in Appendix A.

The model consist in patches  $x_\nu$  of the microwave sky at frequency  $\nu$  (143, 217 and 353 GHz in this work), each one composed by a linear combination of  $c$  astrophysical components with  $e_\nu$  emission maps convolved with the instrumental beam of the experiment  $i_\nu$  plus instrumental noise  $n_\nu$ , that is

$$x_\nu = i_\nu * e_\nu + n_\nu, \quad (2)$$

where the symbol  $*$  denotes convolution. Moreover, the emission maps are a superposition of different astrophysical components, each one with a particular non-linear spectral behavior. Their superposition can be written as a linear combination of each foreground

$$e_\nu = \sum_c A_{c,\nu} s_c, \quad (3)$$

where  $A$  is called the "mixing matrix" and  $s$  is the vector of components. Therefore, equation (2) becomes

$$x_\nu = i_\nu * \left( \sum_c A_{c,\nu} s_c \right) + n_\nu. \quad (4)$$

In the first epoch, the parameters of the model are randomly initialize, and the neural network "reads" in its first convolutional block a tensor formed by a matrix of  $N_{pix} \times N_{pix} \times \nu$ , where  $N_{pix} = 256$  is the number of pixels and  $\nu$  is the number of frequency channels. Then, the spectral dimension of the input data is considered by estimating a multidimensional strided convolution (Goodfellow 2010)

$$H_{\nu,i,j} = \sum_{k,m} W_{k,m,i} V_{s \circ \nu + k,m,j}, \quad (5)$$

where  $H$  are the hidden units (i.e related to the resulting outputs in the first convolutional block), which indexes each spectral dimension  $\nu$  within feature map  $i$  for sample  $j$ .  $W$  is the kernel, which connects for each spectral channel the weights between  $i$  and  $j$ .  $V$  are the visible units (i.e related to the input images), which have the same format as  $H$ . The subindex  $s$  represents a vector of strides, which are the number of pixels shifts over the input matrix. Since in our case are  $s = 2$  on every layer, the network move the filters to 2 pixels at a time on each layer. The symbol  $\circ$  represents the elementwise product. The next convolutional blocks have similar operations but they consider as inputs the information computed in their previous convolutional block.

In the deconvolutional blocks, the spectral dimension of data are considered by computing a multidimensional transpose of strided convolution

$$R_{q,m,j} = \sum_{\nu,k|d \circ c + k = q} \sum_i W_{k,m,i} H_{c,i,j}, \quad (6)$$

where  $R$  are the hidden units in the deconvolutional block and  $H$  the visible ones (i.e the information from the previous block). The symbol  $|$  denotes the modulus operator. The other terms are the same defined in Equation (5). The kernel values  $W$  in all convolutional and deconvolutional blocks will be updated on each epoch after minimising the mean squared error loss function

$$MSE = \frac{1}{2} |y - y'|^2, \quad (7)$$

where  $y$  is the value predicted by the model and  $y'$  is the true value, which in our case is the map with the true CMB emission. This function is located at the end of the architecture and, after computing it, a gradient is then estimated. Once the gradient is computed, the parameters for each layer become updated as it is explained in Appendix A. In the last deconvolutional block, all the spectral information of its previous block is deconvolved into a single channel in order to predict the CMB signal at  $\nu_0 = 217$  GHz, that is, the network computes the quantity  $R_{q=\nu_0,m,j}$  by indexing  $H_{c,i,j}$  in Equation (6) over all the filters  $c$  on the previous deconvolutional block, producing the quantity

$$\tilde{x}_{\nu_0} = i_{\nu_0} * e_{CMB,\nu_0} + \tilde{n}, \quad (8)$$

that is, we obtain a map  $\tilde{x}_{\nu_0}$  at  $\nu_0$  frequency composed by the  $e_{CMB,\nu_0}$  CMB emission convolved with  $i_{\nu_0}$  (i.e the instrumental beam of the experiment) plus  $\tilde{n}$ , which is generalised noise due to deconvolution.

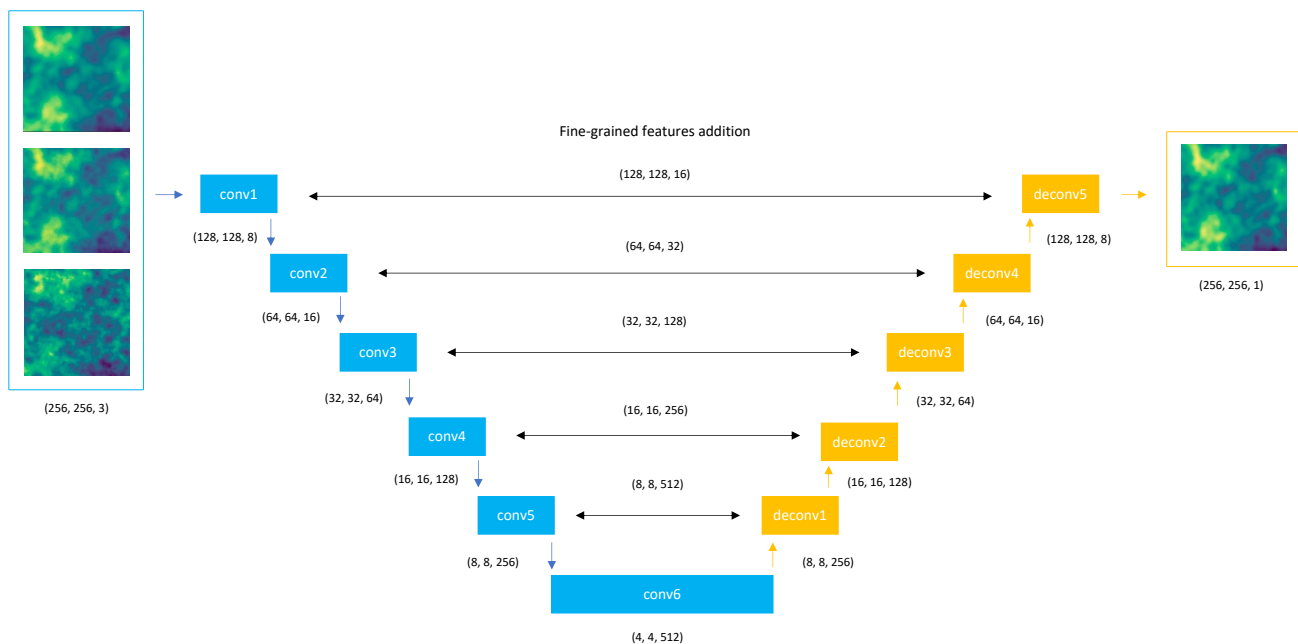


**Fig. 2.** Architecture of CENN. It has a convolutional block which produces 8 feature maps. After that, the space dimensionality increases to 512 feature maps through five more convolutional blocks. These layers are connected to deconvolutional blocks which decrease the space dimensionality to 1 feature map in the last deconvolutional one. Fine-grained features are added from each convolution to its corresponding deconvolution.

### 3.2. Architecture

Our topology is a FCN based on the U-Net architecture (Ronneberger et al. 2015). The inputs of the network are three patches ( $256 \times 256$  pixels) with the total sky emission, one for each frequency at the same position. The output is a single patch, with the same size of the input ones, containing the recovered CMB signal. The label for minimising the loss function is the true CMB signal on each simulation. The network is trained during 500 epochs with 60 000 simulations divided into minibatches of 32.

The architecture of CENN is shown in Figure 2 and is detailed as follows: firstly, it has a set of six convolutional blocks, all of them formed by convolutional and pooling layers with 8, 2, 4, 2, 2 and 2 kernels of sizes of 9, 9, 7, 7, 5 and 3 respectively. The number of filters is 8, 16, 64, 128, 256 and 512 respectively. They have a subsampling factor of 2. The padding type "Same" is added in all the layers in order to add some "space" around the input data or the feature map, to deal with possible loss in width and/or height dimension in the feature maps after having applied the filters. The activation function is leaky ReLU in all the layers. Secondly, the FCN has a set of six deconvolutional blocks, which are formed by deconvolutional and pooling layers with 2, 2, 2, 4, 2 and 8 kernels of sizes of 3, 5, 7, 7, 9 and 9 respectively. The number of filters is 256, 128, 64, 16, 8 and 1. Their subsampling factor is 2. The padding type "Same" is also added in all the layers and the activation function is the leaky ReLU.

In order to take into account fine-grained features in the image (Wei et al. 2021) we have added layers into the architecture, connecting both convolutional and deconvolutional blocks. This addition doubles the space of the feature maps before each deconvolutional block. The main goal for these layers is to help the network to predict low-level features with the deconvolutional

blocks by taking into account high-level ones inferred by the convolutional ones. After each fine-grained layer, a deconvolutional block is connected in order to predict patterns that are dependent on both high and low-level features. In our model, the addition of these layers is related to the task of predicting small-scale regions of the CMB signal by taking into account large-scale structures already inferred. An example of CENN output patches are shown in Figure 1, third column.

## 4. Results

Once CENN is trained, we validate it both using a dataset of 6 000 simulations of random patches at all sky, and using three different validation datasets of 2 000 simulations each set at different latitude ranges: the first one at  $0^\circ < |b| < 5^\circ$ , the second one at  $5^\circ < |b| < 30^\circ$  and the third one at  $30^\circ < |b| < 90^\circ$ . All the validation datasets consist of simulations different from the training one and, in particular, the CMB signal is from another PLA simulation. The analysis of the results is split into three parts: firstly, in Section 4.1 we study the CMB power spectrum at all sky. Secondly, in Section 4.2 we analyse both the mean residuals and the residuals of the mean patch in the all sky case and in the three latitude intervals. Thirdly, in Section 4.3 we estimate the levels of contamination at small scales.

### 4.1. Power Spectra

In Figure 3 we compare, at the top panel, the power spectrum of the true CMB maps against the one from the outputs of CENN, validated over all sky. More precisely, we compare the average of the power spectra computed on the input (blue line) and output (red line) sky patches. The re-binning for the power spectrum is

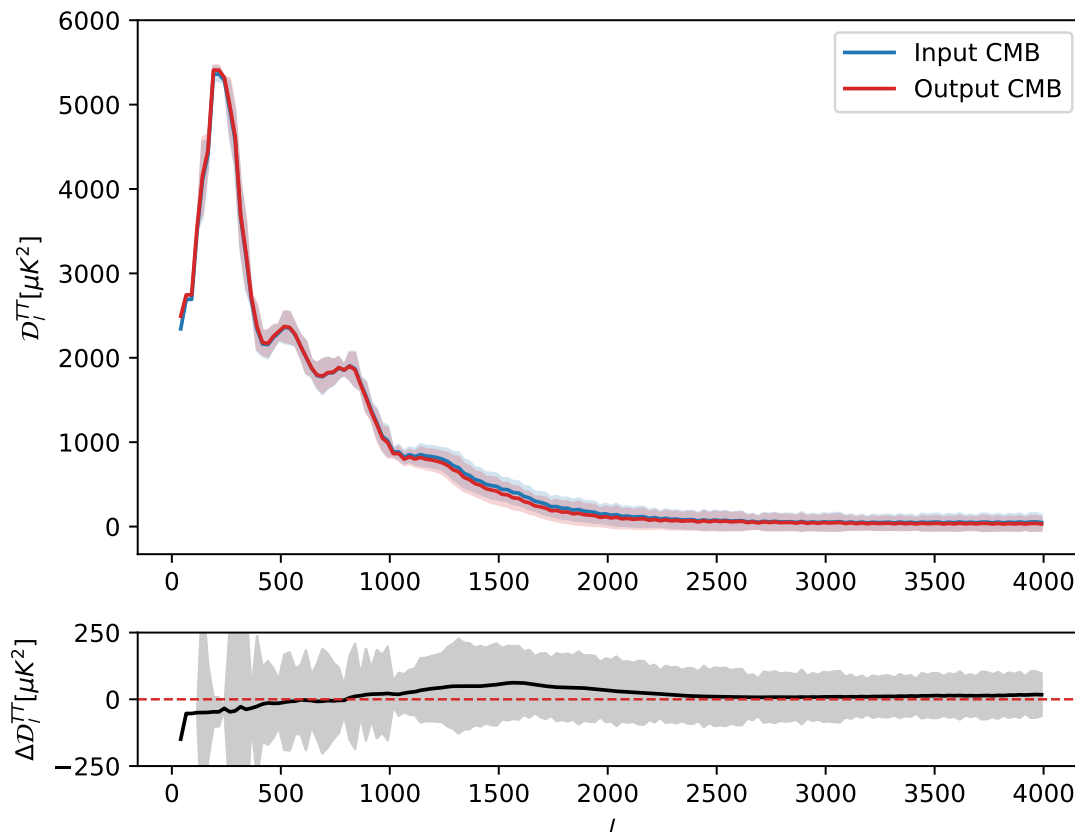


**Fig. 3.** Mean CMB power spectrum comparison computed over the entire validation dataset. The true CMB is represented as a blue line and the output from CENN is shown as a red line. The corresponding uncertainties, computed as the standard deviation of each bin, are the blue and red areas respectively. The difference between input and output is plotted in the bottom panel as a black line, and its uncertainty is the gray area.

done using a step of 50 up to  $l = 1\,000$  and a step of 200 above  $l > 1\,000$ . The standard deviation of each bin for the input and output patches is also shown (blue and red areas respectively), which is considered the uncertainty of each quantity. Furthermore, the bottom panel shows the difference between the input and the output average power spectra (black line) and its uncertainty (gray area).

We recover the CMB power spectrum with a mean difference between input and output of  $13 \pm 113 \mu K^2$  for all multipoles and  $-18 \pm 150 \mu K^2$  for multipoles up to  $l \sim 1\,000$ . In Petroff et al. 2020, they recover the CMB with a difference of  $3.8 \mu K^2$  up to the same multipoles after masking map pixels with a predicted standard deviation of  $>50 \mu K^2$ , being this a per-pixel error comprising both statistical and model uncertainties, while this is not the case of this work. However, in our model, we are testing CENN without the use of any pixel mask. At the first multipoles the CMB cannot be properly recovered due to the fact that we are working with patches of the sky, so we have poor statistics at the largest angular scales. Moreover, between  $l \sim 1\,000$  and  $l \sim 2\,500$ , we obtain a CMB power spectrum with a difference of  $20 \pm 100 \mu K^2$  with respect to the input data, while in Petroff et al. 2020, they obtain a mean value above  $100 \mu K^2$ . This result is interesting mostly because the traditional component separation methods applied to *Planck* data (Planck Collaboration et al. 2020b) also failed at these multipoles and they need to mask the Galactic region and the brightest PS, to avoid such contamination. Our method can be used to recover the CMB at all sky, without applying any sky mask at all. It means that, on the one hand, we are successfully recovering the CMB signal even in the region mostly affected by galactic emission and generally avoided

by traditional component separation methods. On the other hand, the fact that we do not need to mask the PS allows us to successfully recover the signal also at large angular scale. Therefore, it is quite likely that our network will recover the CMB signal with satisfying accuracy and reliability in future CMB experiments with better angular resolution than *Planck*.

#### 4.2. Residuals

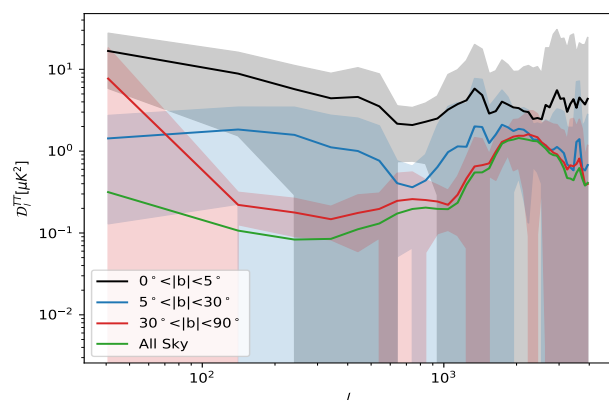


**Fig. 4.** Power spectrum of the mean residual patches for all sky (green continuous line) and for  $0^\circ < |b| < 5^\circ$  (black continuous line),  $5^\circ < |b| < 30^\circ$  (blue continuous line),  $30^\circ < |b| < 90^\circ$  (red continuous line). The corresponding coloured areas are the standard deviation of each bin.

**Table 1.** Mean value of the residual patch (top row) and its root mean squared value (bottom row) for each sky latitude and for all sky.

	$0^\circ < b < 5^\circ$	$5^\circ < b < 30^\circ$	$30^\circ < b < 90^\circ$	All sky
Mean residual patch ( $\mu K$ )	5.072	-0.026	5.238	-0.83
RMS residual patch ( $\mu K$ )	7.732	7.536	6.85	7.372

In this section, we study the mean power spectrum of the residual maps (i.e. the difference between input CMB and CENN output patches) and the power spectrum of the mean residual patch. Firstly, we compute the mean and the root mean squared (RMS) of the residual patch for the whole sky, and for the three different latitude intervals. Table 1 lists the mean value (top row) and the RMS value (bottom row) for  $0^\circ < |b| < 5^\circ$  (second column),  $5^\circ < |b| < 30^\circ$  (third column),  $30^\circ < |b| < 90^\circ$  (fourth column) and the whole sky (fifth column).

The mean value is  $5.072 \mu K$  for the inner Galactic region, a close value to the one for the extragalactic one,  $5.238 \mu K$ . At intermediate latitudes, the mean value is  $-0.026 \mu K$ . Finally, when the whole sky is taken into account, we obtain a mean value of  $-0.83 \mu K$ . For the RMS, we obtain  $7.732 \mu K$  for the Galactic region and  $7.536 \mu K$  for the intermediate one, which is a lower number than the one in Leach et al. 2008 for some of the component separation methods used in *Planck*. More precisely, they presented a RMS value of about 15 and  $13 \mu K$  for SMICA and 18 and  $16 \mu K$  for SEVEM for the respectively latitude intervals both by using realistic simulations.

In Figure 4, we compare the power spectrum of the mean residual patch, that is, firstly we compute the mean residual patch for each validation dataset, and after that we estimate its power spectrum. This kind of study is not only useful for comparison against other segmentation methods but also it allow us to improve our statistical knowledge of the method, for example identifying possible systematic biases such as artifacts near the borders which are common for methodologies working with patches.

As we can see, the residuals are lower than  $15 \mu K^2$  for multipoles up to  $l \sim 4\,000$ . In the inner Galactic region, the strong contamination implies  $7 \pm 25 \mu K^2$ , that is, only a higher residuals for all multipoles with respect to the other cases. This is an important achievement because this is a region usually avoided when adopting more traditional component separation methods.

In the intermediate case we can see that, although it is still a region with high Galactic contamination, our method is well performing, obtaining residuals of about  $2 \pm 10 \mu K^2$  for multipoles up to  $l \sim 4\,000$ . As in the inner Galactic case, this region was usually partially masked by the component separation methods used in *Planck*. Finally, in the extragalactic region, the power spectrum of the mean residual patch shows the expected behavior: in the overall it has lower values since in this region the Galactic contamination is significantly low with respect to the other cases.

The residual behavior remains almost constant even at high multipoles. More precisely, for  $l > 1\,000$ , we obtain values of about  $3 \pm 11 \mu K^2$  for  $0^\circ < |b| < 5^\circ$ ,  $1 \pm 2 \mu K^2$  for  $5^\circ < |b| < 30^\circ$ ,  $0.5 \pm 0.6 \mu K^2$  for  $30^\circ < |b| < 90^\circ$  and  $0.8 \pm 1.5 \mu K^2$  for all sky, which are still a low values for the residuals. This suggests that, in principle, masking might not be needed with our network which gives us the advantage of not having to deal with the holes left by PS masks in CMB reconstructed maps. The performance at these multipoles is probably due to the fact that the network is trained to segmentate diffuse signals, which have a completely different characteristics than the point-like ones. Then, the model

extract the CMB signal being slightly affected to PS contamination.

In Figure 5 we compare the mean power spectrum (black line) of each residual patch in the validation datasets against the input and recovered CMB signal and the level of contamination of each foreground in the simulations (the thermal Sunyaev-Zel'dovich effect appears in the 143 and 353 GHz input simulations during validation, but, since the output is at 217 GHz, the contribution is neglected). The corresponding uncertainties for each quantity (i.e. the standard deviation, as in the above subsection) are represented as coloured areas.

As it is shown, the residuals depend strongly on contamination levels. In the Galactic plane region, we obtain residuals of about  $700 \pm 60 \mu K^2$ . In the other Galactic region, residuals decrease to  $80 \pm 30 \mu K^2$ . However, the contamination levels in these regions are about 3 and 2 orders of magnitude higher, respectively. In the extragalactic region, the impact of contaminants is not as higher as in the other cases, and so on the residuals, which are above  $30 \pm 20 \mu K^2$ . Finally, with random simulations at all sky, we obtain residuals of about  $20 \pm 10 \mu K^2$ , although we can see that we have almost 2 orders of magnitude of contamination levels.

At small scales, in all cases, the residuals show a little bump, which could also seen in Figure 4, due mainly to extragalactic foregrounds. However, it should be noted that for multipoles  $l > 2500$ , where the *Planck* beam made the foregrounds decrease, the residuals remain constant and at lower levels with respect to the large scales. As Figure 5 shows with the brown continuous line, in this region the instrumental noise is strong, though. This is the first indication that these kind of ML models could deal with instrumental effects. This behavior of CENN should be studied in details and tested in future works since constraining both instrumental and systematics effects is crucial for primordial B mode detection.

#### 4.3. Contamination at small scales

In this subsection we focus on the study of the performance of the network against contamination at small scales by analysing a specific patch that has been selected for its visual much higher contamination at small scales with respect to the average case. The patch is represented in the top subfigure in Figure 6 (units in  $\mu K$ ): from left to right, the total patch with all the contaminants and the CMB added together, the input CMB for the same patch, the network output and the residual (the difference between the input CMB and the output) patches.

The small scale structure can be seen in the pixels [237, 41], [100, 70] [169, 148] [80, 185], mostly in the residual patch. Despite the high contamination, the residuals are relatively low, being the mean value  $-0.72 \pm 15.52 \mu K$ . The highest and lowest values that can be also seen by eye in the residual patch correspond to point like objects which contaminate the network output at small scales. In particular the pixels at [237, 41] are the brightest ones in the input total patch with a value of about  $1\,000 \mu K$ . This point-like structure is still present in the output patch with a value lower than  $300 \mu K$  and it is clearly visible in the residual patch with absolute values of about  $100 \mu K$ . Such numbers

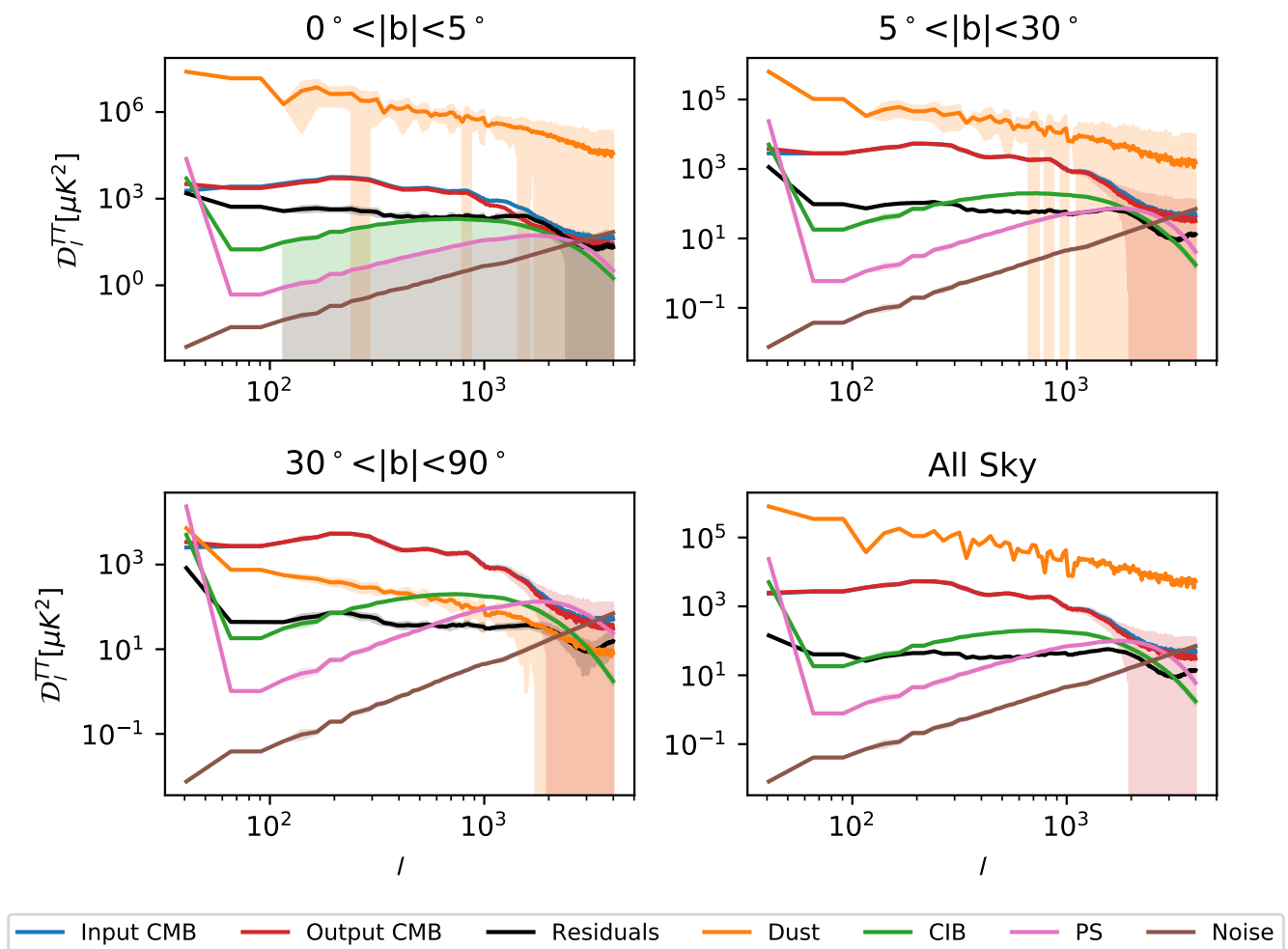


**Fig. 5.** Mean power spectrum of the residuals (black) and its uncertainty (gray area) for  $0^\circ < |b| < 5^\circ$  (top left panel),  $5^\circ < |b| < 30^\circ$  (top right panel),  $30^\circ < |b| < 90^\circ$  (bottom left panel) and for all sky (bottom right panel) against the input and output CMB (blue and red lines respectively) and their uncertainties (blue and red areas respectively). In all cases, the uncertainties are the standard deviation of each bin. It is also represented the contribution of each foreground in the simulations through their power spectra, being the thermal dust represented by the orange line, the PS and CIB the pink and green lines respectively, and the instrumental noise the brown one.

suggests that the network is still well performing even for such problematic patch, since the contamination from the small scales is notably reduced.

In the bottom subfigure in Figure 6 we also compare the power spectra of the input, output and residual patches of this sky area. The re-binning has a step of 50 till  $l < 1\,000$ , and a step of 200 above  $l = 1\,000$ . In the top panel we represent both the input and the output CMB power spectrum as blue and red lines respectively with their uncertainties, estimated as the standard deviation, plotted as blue and red areas respectively. In the middle panel, we show the difference between input and output power spectra with the gray area being the uncertainty. In the bottom panel, we plot the power spectrum of the residual patch, being the green area the uncertainty.

As we show, CENN recover the CMB power spectrum with a mean difference between 0 and  $30\ \mu\text{K}^2$  (black line) for all the range of multipoles. In particular, between  $l = 1\,200$  and  $l = 1\,800$ , the difference between input and output is higher, with a value of about  $50\ \mu\text{K}^2$ . The estimated power spectrum of the residuals (green line) at the same multipoles, has  $40\ \mu\text{K}^2$ , decreasing at higher multipoles.

So, applying our network without any mask, the residual PS affect slightly the network output, but mainly at multipoles around 2 000. The residuals at higher multipoles are negligible and there is no residual contamination with the instrumental noise, at least at the *Planck* noise level. Moreover, we test the performance of the network in patches with both five and ten times higher instrumental noise than the *Planck* one, finding that the performance at high multipoles is similar among the three cases, being the error almost negligible. This behavior is very different from the traditional component separation methods for which above a certain multipole,  $l > 2\,500$ , the power spectrum is completely dominated by the PS and instrumental noise residuals, even after a masking procedure.

## 5. Conclusions

In this work, we develop a new component separation method based on artificial neural networks for future CMB experiments. More precisely, we train a fully convolutional neural network called the Cosmic microwave background Extraction Neural Network (CENN) with realistic simulations of the central channels of the *Planck* mission to extract the CMB signal in total in-

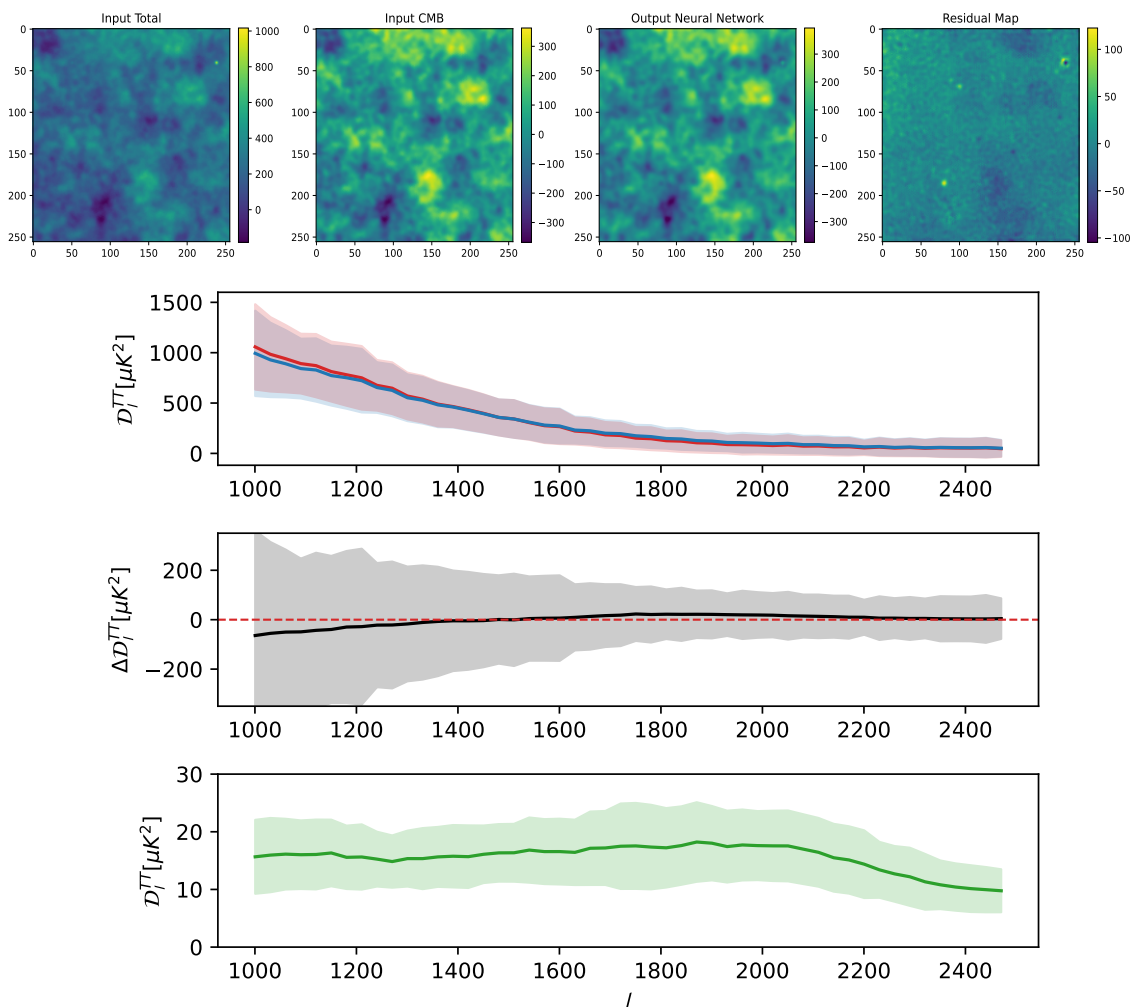


**Fig. 6.** Top subfigure: sky patch selected with high contamination at small scales. The patches represent, from left to right, all the emissions, the CMB label, the neural network output and the residual map computed as the difference between the second and the third columns. The frequency for all the patches is 217 GHz and their temperature (in  $\mu K_{CMB}$ ) is shown in their right vertical bars. Bottom subfigure: CMB power spectrum comparison computed over the patch shown in top subfigure. The true CMB is represented in the top panel as a blue line and the output from CENN is shown as a red line. The corresponding uncertainties (i.e the standard deviation) are shown as blue and red areas respectively. The difference ( $\Delta \mathcal{D}_l^{TT}$ ) between input and output is plotted in the middle panel as a black line, and its uncertainty is the gray area. The power spectrum of the residual map is represented as a green line in the bottom panel, with the green area being its uncertainty (also the standard deviation)

tensity from the other foregrounds, which are thermal dust from our Galaxy, the CIB signal, the thermal Sunyaev-Zel'dovich effect, the contribution from PS (radio and infrared late-type galaxies) and instrumental noise. The frequencies are the 143, 217 and 353 GHz channels.

To train CENN, we use 60 000 realistic simulations. Each one have three image patches of area  $256 \times 256$  pixels containing all the emissions and an additional map with only the CMB contribution at 217 GHz, used to make learning that signal by the neural network via the optimizer and the loss function. Apart from this dataset, we have 6 000 simulations to test the network during the training. After the training, we validate the network with different simulations, which have patches of the CMB signal extracted from a different PLA simulation than the one used for training the network. We develop four different validation datasets: one formed by 6 000 random simulations at all sky, and another three with 2 000 simulations each set at  $0^\circ < |b| < 5^\circ$ ,  $5^\circ < |b| < 30^\circ$  and  $30^\circ < |b| < 90^\circ$  degrees of latitude. After validating CENN, we analyse the results by rebining the data and computing the mean power spectra of both the input and the output CMB from the neural network, and the difference between

them, in all cases considering the standard deviation as the uncertainty of each bin. We obtain a mean difference of  $13 \pm 113 \mu K^2$  for multipoles up to above 4 000.

We compute the mean power spectrum of the residuals (i.e the difference between input and output CMB), obtaining  $700 \pm 60 \mu K^2$  for  $0^\circ < |b| < 5^\circ$ ,  $80 \pm 30 \mu K^2$  for  $5^\circ < |b| < 30^\circ$  and  $30 \pm 20 \mu K^2$  for  $30^\circ < |b| < 90^\circ$ . We also analyse the mean and standard deviation patches for each latitude and for all sky. We obtain a RMS value of  $7.732 \mu K$  for  $0^\circ < |b| < 5^\circ$ ,  $7.536 \mu K$  for  $5^\circ < |b| < 30^\circ$ ,  $6.85 \mu K$  for  $30^\circ < |b| < 90^\circ$  and  $7.372 \mu K$  for all sky. Furthermore, we compute their power spectrum, obtaining  $7 \pm 25 \mu K^2$  for  $0^\circ < |b| < 5^\circ$ ,  $2 \pm 10 \mu K^2$  for  $5^\circ < |b| < 30^\circ$ ,  $2 \pm 3 \mu K^2$  for  $30^\circ < |b| < 90^\circ$ .

Finally, we study the performance of CENN recovering the CMB signal in a patch with high contamination at small scales. We obtain a value of  $50 \pm 250 \mu K^2$  for the difference between input and output CMB power spectra, and residuals of about  $40 \pm 10 \mu K^2$  at multipoles between  $l = 1 200$  and  $l = 1 800$ .

Based on these results, our model is reliable not only at the multipoles analysed in *Planck* ( $l \leq 2 500$ ) but also for higher multipoles. Therefore, it seems to be a promising model to ex-

tract the CMB signal for future experiments with higher angular resolution than *Planck*.

Moreover, it has other advantages: the first one is that our model is evaluated in all the sky without the use of any confidence mask to avoid strong Galactic contamination regions. Therefore, a more realistic CMB map might be obtained with respect to the inpainted version at the Galactic plane used in *Planck*. The second one is that the PS or galaxy cluster contamination is very small affecting the output power spectrum only in a short multipole range around  $l \sim 2\,000$ . These results can be easily upgraded using a dedicated masking scheme or providing information about the PS and galaxy clusters during the training. These potential upgrades are beyond the scope of the current paper and they will be considered for the application of the network to real data.

Both conclusions about the reliability of CENN with the foregrounds at large and small scales might be a first indication that the network would be able to separate the CMB from the foregrounds by learning their non-Gaussian structures (Coulton & Spergel 2019), which could be an advantage of this approach with respect to the traditional ones. Efforts to study the network performance with these non-Gaussian structures will be crucial in order to detect primordial B-modes on polarisation data. However, this is out of the scope of this work and will be considered in future developments. Moreover, our results suggest that CENN might be able to well perform component separation even in single frequency maps, which is worth to be also tested in the future. Lastly, once trained, our model can extract the CMB in microwave maps almost immediately, which is fundamental for future satellites with high amount of data.

As we explained in Section 2, we have trained CENN with realistic simulations from the Planck Sky Model. However, such simulations do not take properly into account the non-Gaussian behaviours of the foregrounds of the microwave sky, especially at the frequencies analysed in this work, where thermal dust is the most significant foreground and it is known to have a strong non-Gaussian behavior. Therefore, our results could be biased by this approximation of the microwave sky when validating it with real data, even if, as commented above, our network seems to rely on such non-Gaussian structures of the different emissions to recover the CMB signal. Since this issue is one of the major limitations of this kind of ML models, in the future the network performance, both in total intensity and polarisation, must be further tested by training it with more realistic simulations, for example the outputs by ForSE (the generative adversarial neural network developed by Krachmalnicoff & Puglisi 2021), which can include small scale non-Gaussian features extended to 12 arcmin.

*Acknowledgements.* We warmly thank the anonymous referee for the very useful and constructive comments on the original manuscript. JMC, LB, JGN, MMC and DC acknowledge financial support from the PGC 2018 project PGC2018-101948-B-I00 (MICINN, FEDER). JMC also acknowledges financial support from the SV-PA-21-AYUD/2021/51301 project. MMC also acknowledges to be granted by PAPI-20-PF-23 and PAPI-21-PF-04 (Universidad de Oviedo). CB acknowledges support from the ASI COSMOS and LiteBIRD Networks (cosmosnet.it), as well as by the INFN INDARK and LiteBIRD grants. JDS, MLS and JDCJ acknowledge financial support from the I+D 2017 project AYA2017-89121-P and support from the European Union's Horizon 2020 research and innovation programme under the H2020-INFRAIA-2018-2020 grant agreement No 210489629.

This research has made use of the python packages `matplotlib` (Hunter 2007), `Keras` (Chollet et al. 2015), and `Numpy` (Oliphant 2006), also the `HEALPix` (Górski et al. 2005) and `healpy` (Zonca et al. 2019) packages.

## References

- Abazajian, K., Addison, G., Adshead, P., et al. 2019, CMB-S4 Decadal Survey APC White Paper
- Ade, P., Aguirre, J., Ahmed, Z., et al. 2019, *Journal of Cosmology and Astroparticle Physics*, 2019, 056–056
- Baccigalupi, C. 2003, *New A Rev.*, 47, 1127
- Bennett, C. L., Bay, M., Halpern, M., et al. 2003, *ApJ*, 583, 1
- Bonavera, L., Suarez Gomez, S. L., González-Nuevo, J., et al. 2021, *A&A*, 648, A50
- Boudet, N., Mutschke, H., Nayral, C., et al. 2005, *ApJ*, 633, 272
- Cai, Z.-Y., Lapi, A., Xia, J.-Q., et al. 2013, *ApJ*, 768, 21
- Carlstrom, J. E., Holder, G. P., & Reese, E. D. 2002, *ARA&A*, 40, 643
- Casas, J. M., González-Nuevo, J., Bonavera, L., et al. 2022, *A&A*, 658, A110
- Chollet, F. et al. 2015, *Keras*
- Coulton, W. R. & Spergel, D. N. 2019, *Journal of Cosmology and Astroparticle Physics*, 2019, 056
- de Zotti, G., Massardi, M., Negrello, M., & Wall, J. 2010, *A&A Rev.*, 18, 1
- Delabrouille, J., Betoule, M., Melin, J. B., et al. 2013, *A&A*, 553, A96
- Delabrouille, J., Cardoso, J. F., Le Jeune, M., et al. 2009, *A&A*, 493, 835
- Delabrouille, J., Cardoso, J. F., & Patanchon, G. 2003, *MNRAS*, 346, 1089
- Dole, H., Lagache, G., Puget, J.-L., et al. 2006, *A&A*, 451, 417
- Duchi, J., Hazan, E., & Singer, Y. 2011, *J. Mach. Learn. Res.*, 12, 2121–2159
- Eriksen, H. K., Dickinson, C., Lawrence, C. R., et al. 2006, *New A Rev.*, 50, 861
- Eriksen, H. K., Jewell, J. B., Dickinson, C., et al. 2008, *ApJ*, 676, 10
- Farsian, F., Krachmalnicoff, N., & Baccigalupi, C. 2020, *J. Cosmology Astropart. Phys.*, 2020, 017
- Finkbeiner, D. P., Davis, M., & Schlegel, D. J. 1999, *ApJ*, 524, 867
- González-Nuevo, J., Toffolatti, L., & Argüeso, F. 2005, *ApJ*, 621, 1
- Goodfellow, I. J. 2010, Technical Report: Multidimensional, Downsampled Convolution for Autoencoders, Tech. rep., Université de Montréal
- Goodfellow, I. J., Bengio, Y., & Courville, A. 2016, *Deep Learning* (Cambridge, MA, USA: MIT Press), <http://www.deeplearningbook.org>
- Górski, K. M., Hivon, E., Banday, A. J., et al. 2005, *ApJ*, 622, 759
- Hunter, J. D. 2007, *Computing In Science & Engineering*, 9, 90
- Jeffrey, N., Boulanger, F., Wandelt, B. D., et al. 2022, *MNRAS*, 510, L1
- Krachmalnicoff, N. & Puglisi, G. 2021, *ApJ*, 911, 42
- Krachmalnicoff, N. & Tomasi, M. 2019, *A&A*, 628, A129
- Lapi, A., González-Nuevo, J., Fan, L., et al. 2011, *ApJ*, 742, 24
- Lapi, A., Shankar, F., Mao, J., et al. 2006, *ApJ*, 650, 42
- Leach, S. M., Cardoso, J. F., Baccigalupi, C., et al. 2008, *A&A*, 491, 597
- LeCun, Y., Boser, B., Denker, J. S., et al. 1989, *Neural Computation*, 1, 541
- Lecun, Y., Bottou, L., Bengio, Y., & Haffner, P. 1998, *Proceedings of the IEEE*, 86, 2278
- Long, J., Shelhamer, E., & Darrell, T. 2015, in *Proceedings of the IEEE conference on computer vision and pattern recognition*, 3431–3440
- Martínez-González, E., Diego, J. M., Vielva, P., & Silk, J. 2003, *Monthly Notices of the Royal Astronomical Society*, 345, 1101
- Meny, C., Gromov, V., Boudet, N., et al. 2007, *Astron. Astrophys.*, 468, 171
- Negrello, M., Clemens, M., Gonzalez-Nuevo, J., et al. 2013, *MNRAS*, 429, 1309
- Oliphant, T. 2006, *NumPy: A guide to NumPy*, USA: Trelgol Publishing, [Online; accessed <today>]
- Paradis, D., Bernard, J.-P., Meny, C., & Gromov, V. 2011, *Astronomy and Astrophysics*, 534
- Peebles, P. J. E. & Yu, J. T. 1970, *ApJ*, 162, 815
- Petroff, M. A., Addison, G. E., Bennett, C. L., & Weiland, J. L. 2020, *The Astrophysical Journal*, 903, 104
- Planck Collaboration, Adam, R., Ade, P. A. R., et al. 2016a, *A&A*, 594, A10
- Planck Collaboration, Adam, R., Ade, P. A. R., et al. 2016b, *A&A*, 594, A9
- Planck Collaboration, Ade, P. A. R., Aghanim, N., et al. 2016c, *A&A*, 594, A26
- Planck Collaboration, Aghanim, N., Akrami, Y., et al. 2020a, *A&A*, 641, A1
- Planck Collaboration, Akrami, Y., Ashdown, M., et al. 2018, *arXiv e-prints*, arXiv:1807.06208
- Planck Collaboration, Akrami, Y., Ashdown, M., et al. 2020b, *A&A*, 641, A4
- Ronneberger, O., Fischer, P., & Brox, T. 2015, *Medical Image Computing and Computer-Assisted Intervention – MICCAI 2015*
- Rumelhart, D. E., Hinton, G. E., & Williams, R. J. 1986, *Nature*, 323, 533
- Schneider, P. 2006, *Extragalactic Astronomy and Cosmology* (Berlin, Heidelberg: Springer Berlin Heidelberg)
- Smoot, G. F., Bennett, C. L., Kogut, A., et al. 1992, *ApJ*, 396, L1
- Sugai, H., Ade, P. A. R., Akiba, Y., et al. 2020, *Journal of Low Temperature Physics*, 199, 1107
- Toffolatti, L., Argüeso, F., de Zotti, G., et al. 1998, *MNRAS*, 297, 117
- Tucci, M., Toffolatti, L., de Zotti, G., & Martínez-González, E. 2011, *A&A*, 533, A57
- Wang, G.-J., Shi, H.-L., Yan, Y.-P., et al. 2022, *ApJS*, 260, 13
- Wei, X.-S., Song, Y.-Z., Mac Aodha, O., et al. 2021, *IEEE Transactions on Pattern Analysis and Machine Intelligence*
- Zonca, A., Singer, L. P., Lenz, D., et al. 2019, *Journal of Open Source Software*, 4, 1298

## Appendix A: Learning process of CENN

Kernels and filters cited in section 3.1 are adjusted on each epoch by updating non-linear parameters  $\theta_{t+1}$  as

$$\theta_{t+1} = \theta_t + \Delta\theta_t, \quad (\text{A.1})$$

where  $\theta_t$  is the parameter of the previous epoch, and

$$\Delta\theta_t = -\alpha g_t, \quad (\text{A.2})$$

where  $g_t$  is the gradient value at the epoch  $t$ . Furthermore,  $\alpha$  is a term which depends on the selected optimization algorithm. Since our training is performed using the adaptive gradient algorithm (AdaGrad, Duchi et al. 2011) the parameter  $\alpha$  in (A.2) varies as

$$\alpha = \frac{\eta}{\sqrt{G_t + \epsilon}}, \quad (\text{A.3})$$

where  $G_t$  is a diagonal matrix at epoch  $t$  for which the diagonal elements correspond with the sum of the squares of the past gradients,  $\epsilon$  is a smoothing term that avoids division by zero and  $\eta$  is the learning rate, with a value of 0.05 in our model.

When all minibatches of the training dataset flow through all the layers, the gradient in equation (A.2) is then computed in the last deconvolutional block by taking the derivative of the mean squared error loss function ( $E$ ) of equation (7) over the output patch  $O_{v_0}$ , where the subindex  $v_0$  represents the frequency channel of the output patch (217 GHz in this work). Therefore, the gradient at the last deconvolutional block is easily estimated by using

$$g_t = \frac{\partial E}{\partial O_{v_0}} = \frac{\partial}{\partial O_{v_0}} \left( \frac{1}{2} |O_{v_0} - l_{v_0}|^2 \right) = |O_{v_0} - l_{v_0}|, \quad (\text{A.4})$$

where  $l_{v_0}$  is the true value (also known as label or target), that is, the signal we want to extract from the maps, which in our case is the CMB. For the previous deconvolutional block, the model uses this value, that is, the gradient of the subsequent block, and the chain rule to update its weights and filters. Therefore, for the previous deconvolutional block the gradients are

$$\begin{aligned} g_{t,W} &= \frac{\partial O_{v_0,LD}}{\partial W_{LD-1}} = \frac{\partial O_{v_0,LD}}{\partial O_{LD-1}} \frac{\partial O_{LD-1}}{\partial W_{LD-1}} = \\ &= g_{t,LD} \frac{\partial O_{LD-1}}{\partial W_{LD-1}} = g_{t,LD} f_{LD-1} \end{aligned} \quad (\text{A.5})$$

$$\begin{aligned} g_{t,f} &= \frac{\partial O_{v_0,LD}}{\partial f_{LD-1}} = \frac{\partial O_{v_0,LD}}{\partial O_{LD-1}} \frac{\partial O_{LD-1}}{\partial f_{LD-1}} = \\ &= g_{t,LD} \frac{\partial O_{LD-1}}{\partial f_{LD-1}} = g_{t,LD} W_{LD-1}, \end{aligned} \quad (\text{A.6})$$

where  $g_{t,W}$  and  $g_{t,f}$  are the gradients used to update the weights and the filters respectively. Note that the final derivatives in equations (A.5) and (A.6) are computed using the fact that a matrix convolution operation is defined as

$$O_{i,j} = \sum_{m=0}^M \sum_{n=0}^N f(i-m, j-n) W(m,n). \quad (\text{A.7})$$

Moreover, the achronyms LD and LD-1 correspond to the last deconvolutional and its previous blocks respectively. The rest deconvolutional blocks have similar expressions. For the convolutional ones, they have the same derivation than (A.5) and

(A.6) to update their corresponding weights and filters respectively. More precisely, for the last convolutional block

$$g_{t,W} = g_{t,FD} f_{LC} \quad (\text{A.8})$$

$$g_{t,f} = g_{t,FD} W_{LC}, \quad (\text{A.9})$$

where the achronyms FD and LC correspond to the first deconvolutional and the last convolutional blocks respectively. For the rest convolutional blocks both filters and weights are updated following the same way as in (A.8) and (A.9).